



Supersonically sprayed iron oxide nanoparticles with atomic-layer-deposited ZnO/TiO₂ layers for solar water splitting

Tae-Gun Kim^{a,1}, Bhavana Joshi^{a,1}, Chan-Woo Park^a, Edmund Samuel^a, Min-Woo Kim^a, Mark T. Swihart^b, Sam S. Yoon^{a,*}

^a School of Mechanical Engineering, Korea University, Seoul, 02841, Republic of Korea

^b Department of Chemical & Biological Engineering and RENEW Institute, University at Buffalo, The State University of New York, Buffalo, NY 14260-4200, USA

ARTICLE INFO

Article history:

Received 25 March 2019

Received in revised form

20 May 2019

Accepted 21 May 2019

Available online 23 May 2019

Keywords:

Fe₂O₃

Supersonic cold spray

Solar water splitting

Atomic layer deposition

ZnO

TiO₂

ABSTRACT

We demonstrate a promising Fe₂O₃/ZnO/TiO₂ photoanode for photoelectrochemical water splitting. Passivation of the Fe₂O₃ surface with thin layers of ZnO and TiO₂ enhances the water splitting photocurrent density of Fe₂O₃. The increased photoelectrochemical activity of the hematite-based structure with heterojunctions, compared to that of bare Fe₂O₃, results from improved charge separation during water oxidation. The multilayered Fe₂O₃ film exhibits a seven-fold improvement in photocurrent density (to 4.25 mA cm⁻²) compared with bare Fe₂O₃, due to suppression of electron–hole recombination. The transient photocurrent density and impedance were evaluated to assess the effect of the passivation layer thickness and achieve a high photocurrent at low potential (0.7 V vs. Ag/AgCl) through improved light harvesting of the Fe₂O₃ film with an ultrathin ZnO/TiO₂ overlayer.

© 2019 Elsevier B.V. All rights reserved.

1. Introduction

Hydrogen generated by renewable and clean solar photoelectrocatalytic splitting of water is of great interest as a sustainable alternative to conventional fuels for chemical energy storage [1]. Photoelectrochemical (PEC) water splitting is viewed as a potential technological solution for achieving a sustainable carbon-neutral energy economy [2]. While Edmond Becquerel discovered PEC water splitting as early as 1839, research interest in this topic increased significantly only after Fujishima and Honda demonstrated in 1972 that TiO₂ can be used as a catalyst for water splitting. However, while TiO₂ and ZnO are well-known catalysts for PEC water splitting, they are limited by only being responsive to UV light. Other semiconducting metal oxides demonstrated for solar water splitting include BiVO₄, WO₃, CuO, and Fe₂O₃ [3]. For efficient solar water splitting, a material band gap in the range of 1.8–2.2 eV is desirable to allow absorbance of sunlight over a substantial fraction of the visible spectrum above the minimum energy

required for water-splitting. The theoretical maximum solar-to-hydrogen (STH) conversion efficiencies of BiVO₄ and Fe₂O₃ are 9.2% and 16.8%, respectively. The use of Fe₂O₃ for water splitting is attractive because of its high potential STH efficiency, abundance, and low cost [4,5].

Hardee and Bard [5] demonstrated that chemical vapor deposition (CVD)-grown Fe₂O₃ can be used as a water-splitting photoanode at wavelengths greater than 400 nm. Fe₂O₃ is a nontoxic and abundant metal oxide with a bandgap of 2.1 eV. This moderate band gap allows it to absorb 40% of incident solar radiation, with a theoretical solar-to-hydrogen conversion efficiency of up to 16.8% [6]. Unfortunately, many limitations of Fe₂O₃ have kept it from realizing this potential. For example, the lifetimes of the photo-generated electrons and holes in Fe₂O₃ are short [7]. Moreover, Fe₂O₃ suffers from poor hole diffusion kinetics, which limit its photoanode performance. Efforts have been made to develop nanostructures that promote faster transport of holes to the Fe₂O₃ surface [8,9]. However, when the excited holes reach the nanostructured Fe₂O₃ surface, defects arising from oxygen vacancies at the electrode/electrolyte interface promote carrier recombination. Hence, thin overlayers of Al₂O₃, Ga₂O₃, or TiO₂ have been explored as passivation layers to protect the Fe₂O₃ film [10,11]. Furthermore,

* Corresponding author.

E-mail address: skyoona@korea.ac.kr (S.S. Yoon).

¹ These authors have contributed equally.

co-catalysts including IrO_2 , Co-Pi , $\text{Co(OH)}_2/\text{Co}_3\text{O}_4$, Ni(OH)_2 , and NiFeO_x have been used on the surface of Fe_2O_3 to improve its photocurrent density (PCD) and Faradaic efficiency [12]. However, many of these materials are toxic, rare, or expensive [13]. An overlayer coating to passivate the Fe_2O_3 surface is essential for ensuring that it exhibits a high PCD. The resulting improvements in its PCD are attributable to minimization of the required overpotential, suppression of hole recombination, and faster hole transfer kinetics [7,8].

Various materials have been used in passivation layers to protect Fe_2O_3 . ZnO is a superior photocatalytic and conducting material and thus suitable for use in PEC applications [14–16]. However, ZnO readily undergoes photocorrosion in aqueous electrolytes. This shortcoming of ZnO can be overcome by depositing a thin film of TiO_2 as a second passivation layer on it.

Steier et al. reported that surface coating can be exploited for extending the space charge region [17]. TiO_2 has been coated as a passivation overlayer on Fe_2O_3 using various processes [11,13,17]. Barreca et al. [13] coated TiO_2 on a Fe_2O_3 layer by atomic layer deposition (ALD); the Fe_2O_3 itself had been deposited by plasma-enhanced CVD. They observed that the $\text{TiO}_2/\text{Fe}_2\text{O}_3$ heterojunction protected the photoelectrodes from corrosion and thus enhanced the PCD. Jeon et al. [11] fabricated hematite nanorods coated with TiO_2 using a chemical process. They noted that the ultrathin TiO_2 overlayer reduced the surface charge. Ahmed et al. [8] introduced a water-based solution method to deposit TiO_2 on Fe_2O_3 . The TiO_2 passivated surface states, resulting in increases in the photovoltage and PCD. Similarly, Yang et al. [14] observed an increased photovoltage after passivation of a hematite surface by ALD-deposited TiO_2 .

ALD produces dense and conformal coatings, which is a requirement for the passivation layer. ALD-coated TiO_2 is also known to improve carrier separation and reduce electron–hole recombination. Further, when a ZnO layer is sandwiched between the Fe_2O_3 and TiO_2 layers, the valence band of ZnO facilitates generation of photoexcited holes [15].

In this work, we report the deposition of Fe_2O_3 films by supersonic cold spraying onto indium-doped tin oxide (ITO) substrates, followed by coating with protective ZnO and TiO_2 overlayers via ALD. The resulting heterojunction films are then used as photoanodes for water splitting. To the best of our knowledge, this is the first instance of the fabrication of Fe_2O_3 films via supersonic cold spraying for use as water-splitting photoanodes. The fabricated films exhibit superior water-splitting performance as well as high stability.

2. Experimental methods

2.1. Deposition of Fe_2O_3

The primary experimental setup used, namely, the cold-spray deposition system, is shown schematically in the left half of Fig. 1. The cold-spray coating system includes an air tank, an inline heater, a supersonic nozzle, an x – y stage, an atomizer, and a syringe pump; the system has been described in greater detail elsewhere [18]. To deposit Fe_2O_3 , a colloidal dispersion was prepared by mixing 2.75 g of Fe_2O_3 (>99%, Sigma-Aldrich) powder in 40 mL of dimethylformamide (DMF, Sigma-Aldrich). A solution of 8 wt% polyacrylonitrile (PAN; Sigma-Aldrich, average M_w of 150,000) in DMF was prepared, and 0.3 mL of it was added to the $\text{Fe}_2\text{O}_3/\text{DMF}$ solution to improve the degree of dispersion. Next, the Fe_2O_3 colloidal solution was placed in a syringe pump and supplied at a flow rate of 1.5 mL min^{-1} . A gas stream, generated by compressing air to 0.4 MPa and heating it to 250°C , was accelerated through a converging–diverging nozzle such that its velocity became

supersonic. This supersonic gas stream was used to atomize the Fe_2O_3 solution and ensure that the Fe_2O_3 particles hit the ITO-coated glass substrate at high speed. The thus-deposited Fe_2O_3 film was then annealed in Ar at 500°C for 120 min in two steps to remove any impurities present. The temperature was increased from room temperature of 20°C – 200°C for 10 min and then to 500°C for 60 min. The rate of temperature increase was 3°C min^{-1} .

2.2. Deposition of ZnO and TiO_2

An ALD reactor (Lucida™ D series ALD system, NCD Tech, Korea) was employed for the conformal deposition of ZnO and TiO_2 . Diethyl zinc (DEZn; EGChem, Korea) and titanium isopropoxide (TTIP; EGChem, Korea) were used as the metal precursors while deionized water was used as the oxygen source. The precursor doses were controlled using the pulse times of computer-controlled air-actuated valves. The DEZn, TTIP, and water vials were held at room temperature, whereas the bubbler and delivery lines were maintained at 78°C . N_2 was used as the carrier gas for the metal precursors as well as for purging the post-reaction byproducts. The thicknesses of the ZnO and TiO_2 layers were controlled by varying the number of coating cycles (N); the deposition rates used were 0.2 and 0.1 nm/cycle, as determined by deposition on a planar substrate. The Fe_2O_3 , $\text{Fe}_2\text{O}_3/\text{ZnO}$, and $\text{Fe}_2\text{O}_3/\text{ZnO}/\text{TiO}_2$ films are denoted as F, FZ (number of ZnO coating cycles ($N_{\text{Zn}} = 150$)), and FZT (ZnO with $N_{\text{Zn}} = 150$ and number of TiO_2 coating cycles ($N_{\text{Ti}} = 120$)), respectively.

2.3. PEC measurements

PEC tests were conducted in 1 M NaOH using a three-electrode cell in which $\text{Fe}_2\text{O}_3/\text{ITO}$ was the working electrode and Pt and Ag/AgCl were the counter and reference electrodes, respectively. A Xe lamp (Newport, Oriel Instruments, USA) with an AM1.5 filter was used for illumination. The intensity of the incident light was adjusted to 100 mW cm^{-2} . Current density measurements were performed under both dark and light conditions through linear sweep voltammetry (LSV) using a potentiostat (VersaSTAT-3, Princeton Applied Research, USA) for potentials ranging from -0.2 to 0.7 V (vs. Ag/AgCl) at a scan rate of 10 mV s^{-1} . The illuminated electrode area was $0.25 \text{ cm} \times 0.25 \text{ cm}$. Electrochemical impedance spectroscopy (EIS) measurements were conducted using the same VersaSTAT-3 potentiostat and three-electrode configuration. The EIS measurements were performed for frequencies of 100 kHz to 100 mHz under both dark and illuminated conditions using a small sinusoidal perturbation potential (amplitude of 10 mV). Fitting was performed using the software program ZSimpWin.

2.4. Material characterization

Water contact angle measurements were performed using a high-resolution charge-coupled device (CCD) camera (Phantom 9.1, Vision Research, Inc.). An optical profiler (NT-1100, Veeco, USA) was used for surface roughness measurements. A Raman spectrometer (Jasco, NRS-3100) was employed to analyze the chemical bonds in the cold-sprayed films. X-ray diffraction (XRD) analysis (D/max-2500, Rigaku, Japan), with $\text{Cu K}\alpha$ radiation for 2θ values of 20 – 65° , was used to elucidate the crystal structure of Fe_2O_3 . The surface chemical compositions of the films were determined using X-ray photoelectron spectroscopy (XPS, X-TOOL, ULVAC-PHI). The surface morphologies of the Fe_2O_3 and ZnO/ TiO_2 -passivated Fe_2O_3 films were determined using high-resolution scanning electron microscopy (HR-SEM, XL30 SFEG, Phillips Co., the Netherlands), which was performed at 15 kV. Transmission electron microscopy (TEM, JEM 2100F, JEOL Inc.) was used to confirm the formation of the ZnO

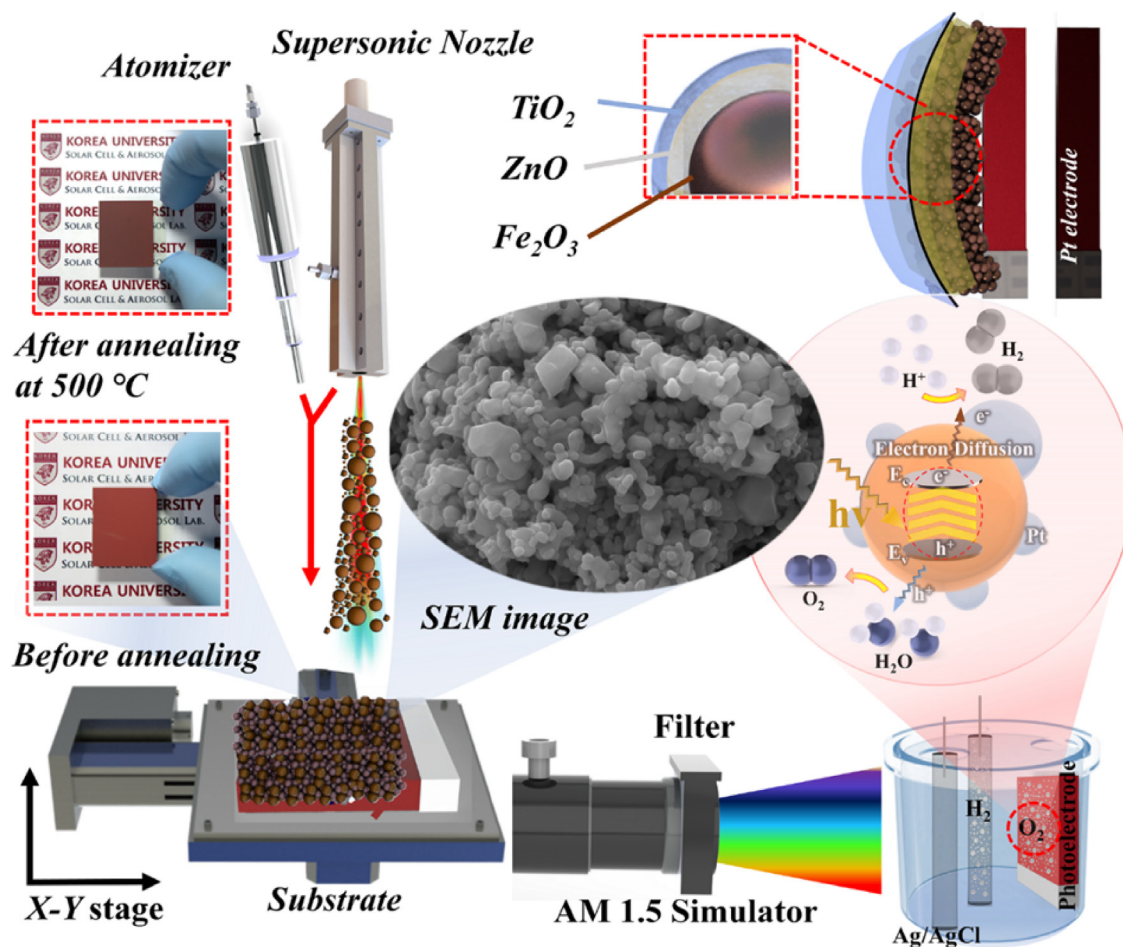


Fig. 1. Schematic of cold-spraying setup, surface morphology of sample as imaged by scanning electron microscopy (SEM), and deposition of ZnO/TiO₂ layers by ALD. Photographs at the top left show Fe₂O₃ films before and after annealing. The image at the top right is a schematic of conformally ALD-coated ZnO/TiO₂ layers over core Fe₂O₃. Fabricated photoanodes were tested using a PEC setup (bottom right). The magnified image illustrates electron–hole generation induced by solar radiation.

and TiO₂ coatings on Fe₂O₃. Cross-sectional samples of the films for the TEM analysis were obtained using a focused ion beam (FIB, 5 nA, LYRA3 XMH, TESCAN) sectioning technique.

3. Results and discussion

Samples F, FZ, and FZT, that is, the Fe₂O₃ layer and the Fe₂O₃/ZnO and Fe₂O₃/ZnO/TiO₂ heterojunction layers were optimized to achieve the highest possible PCD value. Such heterostructures are expected to decrease charge-carrier recombination and increase the surface electrochemical activity at the photoanode/electrolyte interface. The passivation of Fe₂O₃ was confirmed through structural and surface characterization methods, such as Raman spectroscopy, XRD, XPS, SEM, and TEM analyses.

The Raman spectra in Fig. 2 show that the five characteristics peaks of Fe₂O₃ were present in the spectra of all of the samples (A_g modes at 225 and 498 cm⁻¹; E_g modes at 293, 412, and 613 cm⁻¹) [19,20]. The inhomogeneous peak at 656 cm⁻¹ may be attributed to vibrational states of crystal lattice disorder related to hematite [21–23]. The Raman peak observed at 437 cm⁻¹ in the case of sample FZ corresponds to the high-frequency phonon E₂ (high) associated with Zn sublattice vibrations, while that at 549 cm⁻¹ is related to the longitudinal optical component E₁. Furthermore, the Raman spectrum of sample FZT shows peaks characteristic of TiO₂. Raman scattering from TiO₂ was confirmed by the broadening of the peak at 225 cm⁻¹, due to the TiO₂ peak that generally appears at

245 cm⁻¹ and two additional minor peaks at 375 and 556 cm⁻¹. This peak shift may result from low thickness of the TiO₂ layer.

To characterize the surface of the Fe₂O₃ film before and after passivation, water contact angle (WCA, θ_w) measurements were performed using a high-resolution CCD camera. Fig. 3a shows that the θ_w value of the ITO substrate without any coating was 72–74°. The WCA of the ITO substrate indicates that it was in the ideal Wenzel state, wherein the water drops adhered to it [18]. Because Fe₂O₃ is a hydrophilic material [24], the Fe₂O₃ film deposited on the ITO substrate exhibited a WCA of 30–32° (see Fig. 3b), which is half of that of the bare ITO substrate. The formation of the ZnO and TiO₂ coatings increased the WCA to 119–120° (Fig. 3c). As the contact angle increased, the water droplets became more spherical on the substrate surface, reflecting the appearance of a Cassie–Baxter state [18]. These increases in the WCA confirmed that the deposited passivating layers of ZnO and TiO₂ significantly modified the surface of the underlying Fe₂O₃ film. We determined the surface roughnesses of the various samples using an optical profiler; the ITO substrate (Fig. 3d) showed a roughness of 3.86 nm. On the other hand, the Fe₂O₃ layer coated on the ITO substrate showed a reduced roughness (2.26 μm, see Fig. 3e). This property along with the hydrophilic nature of Fe₂O₃ allows the electrolyte to fully wet it, thus stimulating electron–hole recombination in it. However, for the Fe₂O₃/ZnO/TiO₂ (FZT) film, shown in Fig. 3f, the surface roughness was slightly higher at 2.78 μm. The passivating ZnO/TiO₂ layers protect the Fe₂O₃ layers and enhance the PEC performance, but

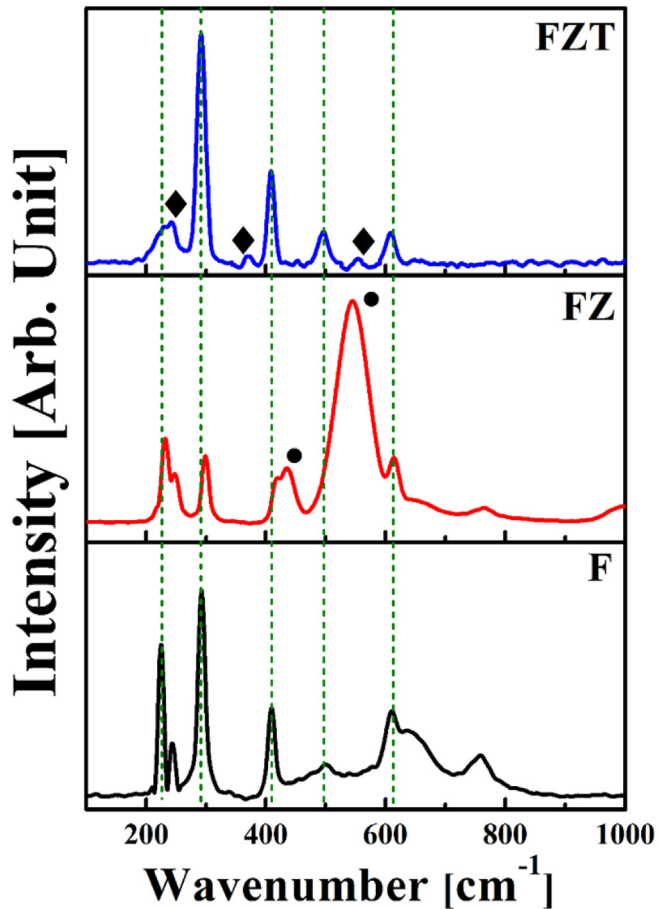


Fig. 2. Raman spectra of samples F, FZ, and FZT. ● indicates characteristic peaks of ZnO while ◆ indicates characteristic peaks of TiO₂.

decrease the wettability of the surface.

Fig. 4a shows the XRD pattern of sample FZT. Diffraction peaks related to the ZnO and TiO₂ layers are absent because of their low thicknesses and amorphous nature. The peaks at 24°, 33°, 35°, 40°, 49°, 54°, 57°, 62°, 64°, and 72° correspond to the (012), (104), (110), (113), (024), (116), (122), (214), (300), and (119) planes of Fe₂O₃ (JCPDS 24-0072). The elemental compositions and bonding states of the various samples were investigated based on the kinetic

energy of the emitted photoelectrons by irradiating their surfaces with X-rays. The full survey spectrum of the Fe₂O₃/ZnO/TiO₂ multilayered film, shown in Fig. 4b, confirms the presence of Fe, Zn, Ti, and O. The doublet peaks at 458.2 and 463.8 eV in the Ti 2p core spectrum can be ascribed to the Ti 2p_{3/2} and Ti 2p_{1/2} states (Fig. 4c). The difference in the binding energies of approximately 5.6 eV indicates the presence of Ti⁴⁺ [25]. In addition, the shoulder peaks at 457.7 and 462.9 eV appear in Ti 2p_{3/2} and Ti 2p_{1/2} that correspond to Ti³⁺ [26]. The Zn 2p core spectrum (Fig. 4d) contains peaks related to the Zn 2p_{3/2} and Zn 2p_{1/2} states at 1044 and 1021.3 eV, respectively, along with the shoulder peak at 1020 eV; the spin-orbit splitting energy of 22.7 eV indicates that Zn exists as Zn²⁺. The Fe 2p core spectrum, shown in Fig. 4e, clearly exhibits peaks at 710.1 and 723.6 eV, which correspond to the Fe 2p_{3/2} and Fe 2p_{1/2} states, respectively. The spin-orbit splitting energy of the two dominant peaks is approximately 13.5 eV, indicating the presence of Fe³⁺, consistent with the Fe₂O₃ phase [27]. The characteristic satellite peak at 719 eV further confirms the presence of Fe₂O₃ [25]. The O 1s spectrum (Fig. 4f) exhibits a peak at 529 eV, which corresponds to metal oxides (M–O) in the multilayered film. When deconvoluted, it reveals peaks centered at 529, 530.3, and 532.2 eV that correspond to M–O, M–O–H and O–H groups. The C 1s XPS spectrum (see Fig. S1), which ranges from 280 to 292 eV, can be deconvoluted into three peaks. The deconvoluted peaks have binding energies of 284.5, 285.8, and 287.8 eV and correspond to sp²-bonded carbon (C–C), carboxylate (C–OH), and carbonyl (C=O), respectively [28].

The surface morphology of the FZT film was observed by SEM and TEM. The high- and low-magnification SEM images in Fig. 5a and b show that the film consisted of particles of various sizes that adhered well to form the film. The particle size distribution, as estimated based on the values for 50 particles, is shown in Fig. 5c and indicates that the particle size was 100–500 nm. Low- and high-resolution TEM images of the FIB-sliced sample are shown in Fig. 5d and e. The HRTEM image (Fig. 5e) displays fringes with d-spacings of 0.269 and 0.16 nm that are attributed to the (104) and (122) planes of α-Fe₂O₃ (JCPDS 24-0072), respectively. The selected-area electron diffraction (SAED) pattern in Fig. 5f shows the diffraction pattern of a single polycrystalline nanoparticle. The pattern can be readily indexed to α-Fe₂O₃, as indicated by the labeled dark-red circles. The many diffraction spots visible in the SAED indicate that the particle is polycrystalline. The HTREM image in Fig. 5g shows thin and distinct contrasting shells, confirming that the ZnO and TiO₂ coatings were formed successfully on the Fe₂O₃ particle film. The number of coating cycles performed for ZnO and TiO₂ on the Fe₂O₃ nanoparticles were $N_{Zn} = 150$ and $N_{Ti} = 120$,

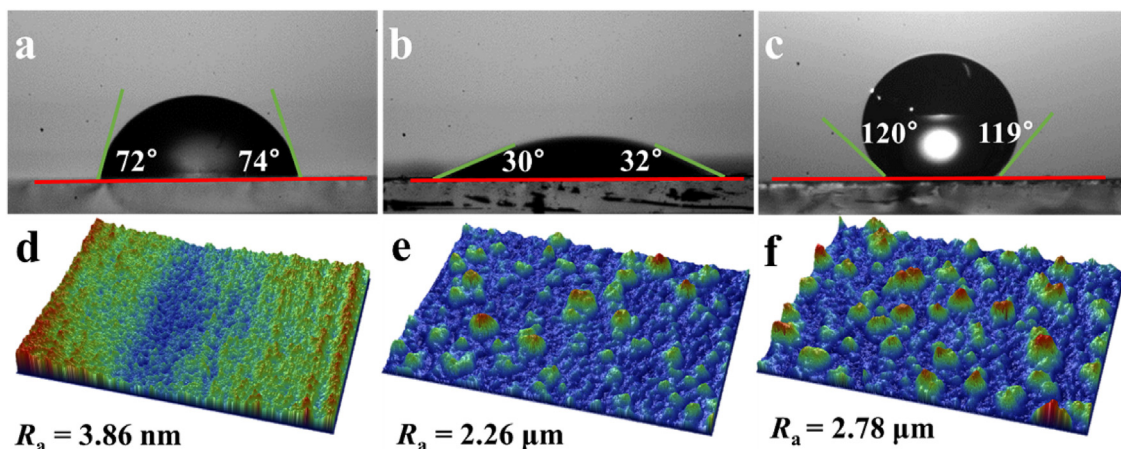
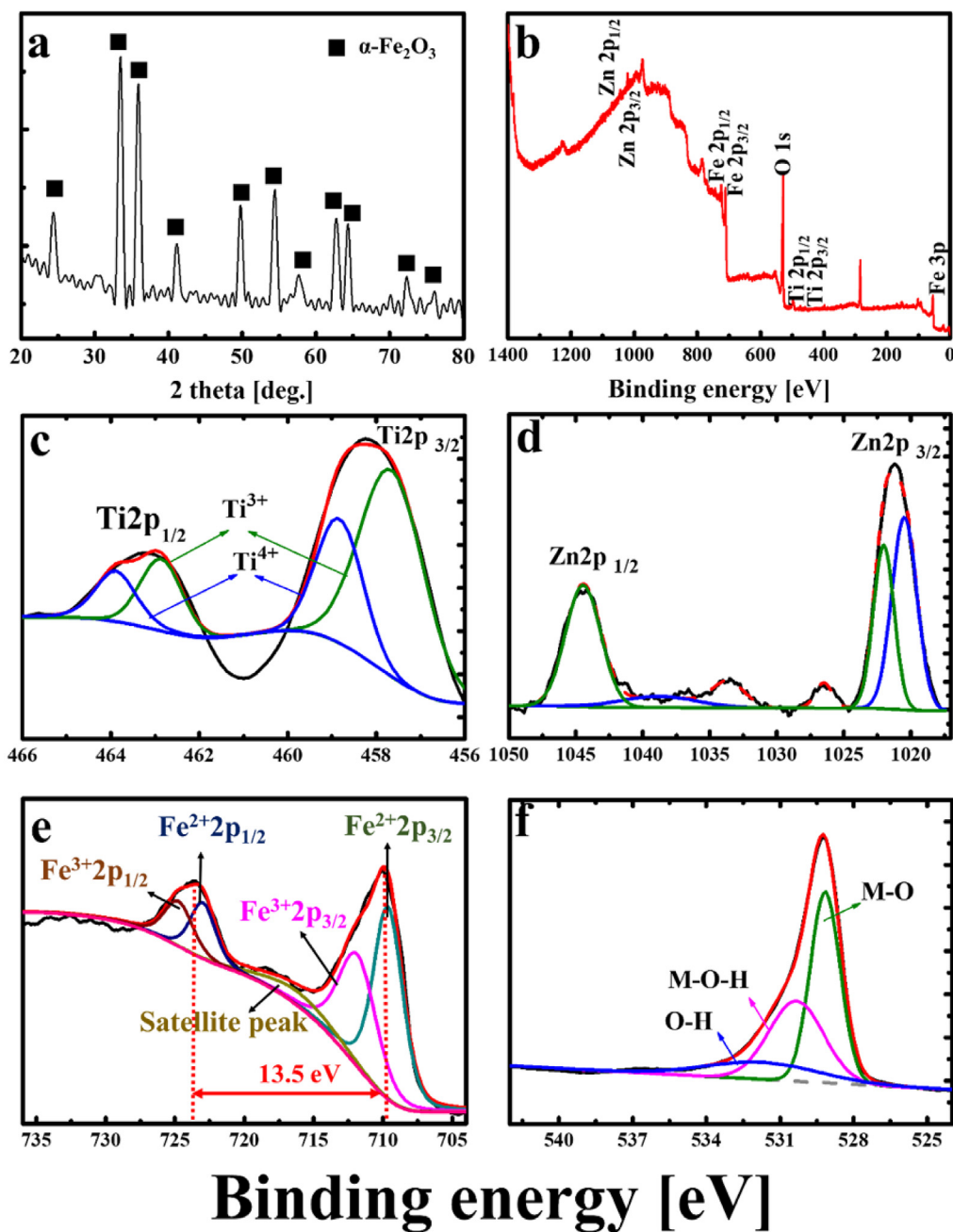


Fig. 3. Water contact angles of (a) ITO substrate and (b) Fe₂O₃ and (c) Fe₂O₃/ZnO/TiO₂ films. Images in (d)–(f) are optical profiles corresponding to samples in (a)–(c), respectively.

Intensity [Arb. Unit]



Binding energy [eV]

Fig. 4. (a) XRD pattern of FZT. (b–f) XPS spectra of sample FZT: (b) full (survey) spectrum, (c) Ti 2p, (d) Zn 2p, (e) Fe 2p, and (f) O 1s spectra.

respectively. The thicknesses of both films were lower than would be expected based on one monolayer of growth per ALD cycle, because of the varying sizes of the Fe_2O_3 particles and the surface roughness of the Fe_2O_3 film (see Fig. 3e). It is well known that the thickness of ALD layers can vary quite significantly over non-uniform surfaces [29]. The grayscale TEM image in Fig. 5g was post-processed to identify the outer layers of ZnO and TiO_2 . We used a MATLAB function to create a colored representation of the layers of FZT in Fig. 5g, confirming the conformal formation of ZnO and TiO_2 layers on the Fe_2O_3 particles. The elemental mapping of other samples is presented and discussed in supporting information; see Fig. S2.

The PEC properties of the cold-sprayed Fe_2O_3 films were analyzed using a three-electrode setup; 1 M NaOH (pH = 14) was

used as the electrolyte and Ag/AgCl was used as the reference electrode. A comparison of the current density curves of samples F, FZ, and FZT is shown in Fig. 6a. Dark current was negligible over this voltage range. Under AM 1.5 illumination, however, the Fe_2O_3 film shows a small photoanodic current of 0.59 mA cm^{-2} at 0.7 V. When the Fe_2O_3 film was coated with a thin layer of ZnO ($N_{\text{Zn}} = 150$), the PCD increased to 2.11 mA cm^{-2} . Further, a thin ALD coating of TiO_2 ($N_{\text{Ti}} = 120$) over $\text{Fe}_2\text{O}_3/\text{ZnO}$ yielded a seven-fold overall increase in the photocurrent at 0.7 V, to 4.25 mA cm^{-2} . The enhanced PCD of FZT is likely owing to the presence of the passivation layers of the two heterovalent semiconducting materials (i.e., ZnO and TiO_2) and the synergistic effect of these passivation layers and Fe_2O_3 . The PCD of Fe_2O_3 is lower because of slow water oxidation kinetics associated with accumulation of holes at the interface; these holes are

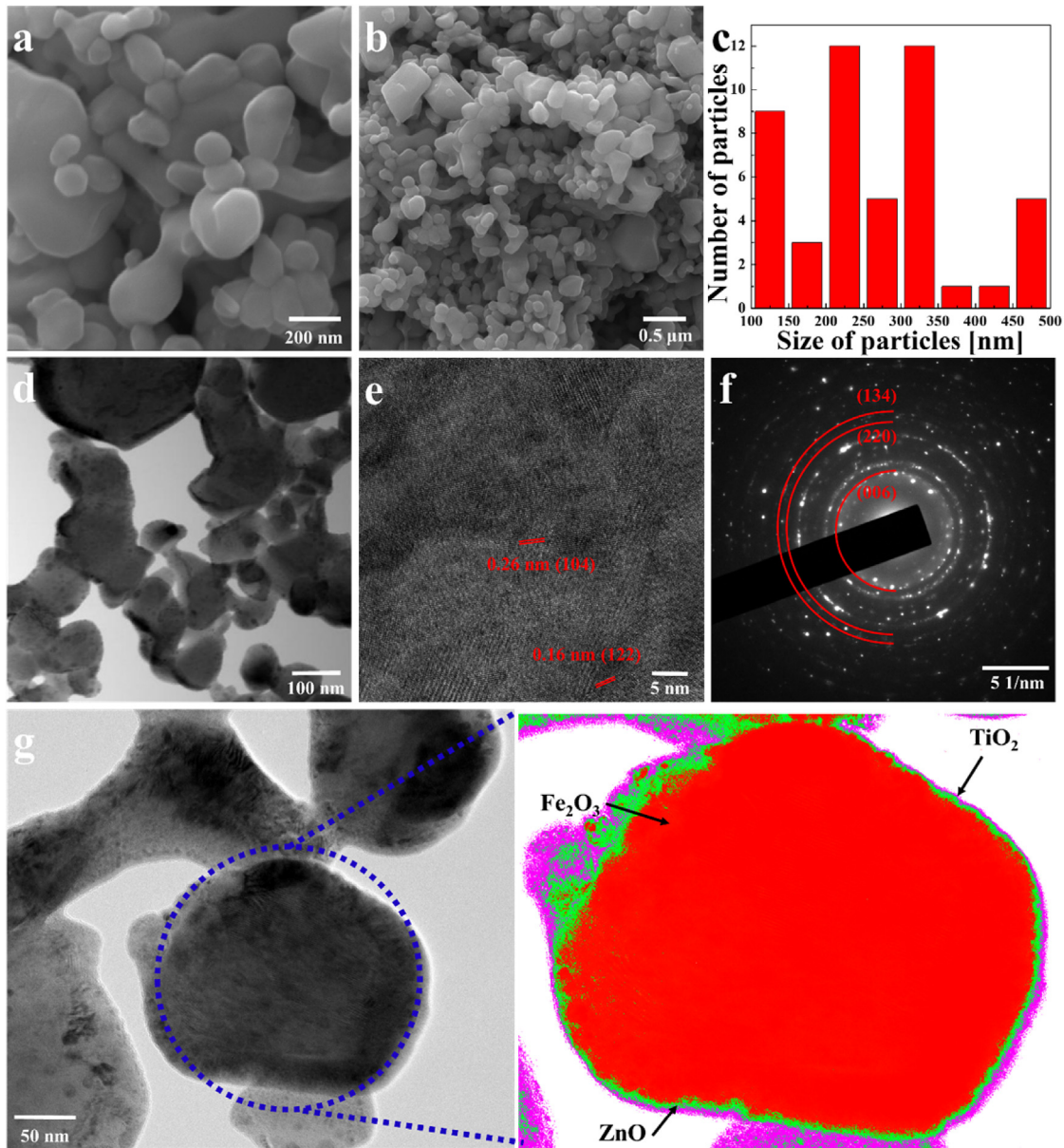


Fig. 5. (a) High-, (b) and low-magnification SEM images showing the surface morphology of the FZT film. (c) ZnO/TiO₂ coated Fe₂O₃ particle size distribution. (d) Low- and (e) high-resolution TEM images of material sectioned from the FZT film. (f) Selected-area electron diffraction (SAED) pattern and (g) high-magnification TEM image of FZT; ZnO/TiO₂-coated Fe₂O₃ particle in (g) is covered by ZnO and TiO₂ layers, as indicated by color scheme (green and purple for ZnO and TiO₂). (For interpretation of the references to color in this figure legend, the reader is referred to the Web version of this article.)

trapped in the case of FZT because of the presence of the ultrathin passivation layers. In addition, with the passivation layer, the reduced barrier potential increases oxygen evolution and mobility of the local carriers which enhances the photocurrent density via photo-excited electron-hole pairs [30]. Initially, the PCD values were measured for different thicknesses of the ZnO layer in order to optimize it. The optimized number of coating cycles for ZnO was $N_{zn} = 150$, as it yielded the highest PCD (2.11 mA cm^{-2}) at 0.7 V. This is an increase of 3.5 times with respect to that of pristine Fe₂O₃. Next, the thickness of the TiO₂ layer formed on the ZnO-coated Fe₂O₃ film was optimized, and the optimal number of coating cycles was determined. Electrons flow more readily in the vertical direction toward Fe₂O₃ in the FZT structure, owing to the thin layers of ZnO/TiO₂. These passivation layers restrict the rapid electron-hole recombination before holes reach the electrode-electrolyte

interface. As presented in Fig. 6b, the PCD value increased gradually with an increase in the number of TiO₂ coating cycles, with the highest value being observed at $N_{Ti} = 120$, and then decreased. This fall in the PEC performance after $N_{Ti} = 120$ can be attributed to the increased electron-transport distance as well as the decrease in the electric field across the layer, which results in increased charge-carrier recombination [31]. The addition of the TiO₂ ($N_{Ti} = 120$) layer increased the surface roughness and protected the Fe₂O₃ and ZnO layers from possible photocorrosion, thus ensuring that the photocurrent of the heterostructured FZT photoanode was not only higher, but also more stable. The PEC performances of these samples is compared with those of previously-reported pristine Fe₂O₃ films and films surface-passivated using layers of other materials (see Table 1). The approach used here, with a ZnO/TiO₂ coating on spray-deposited Fe₂O₃ clearly provides much better performance

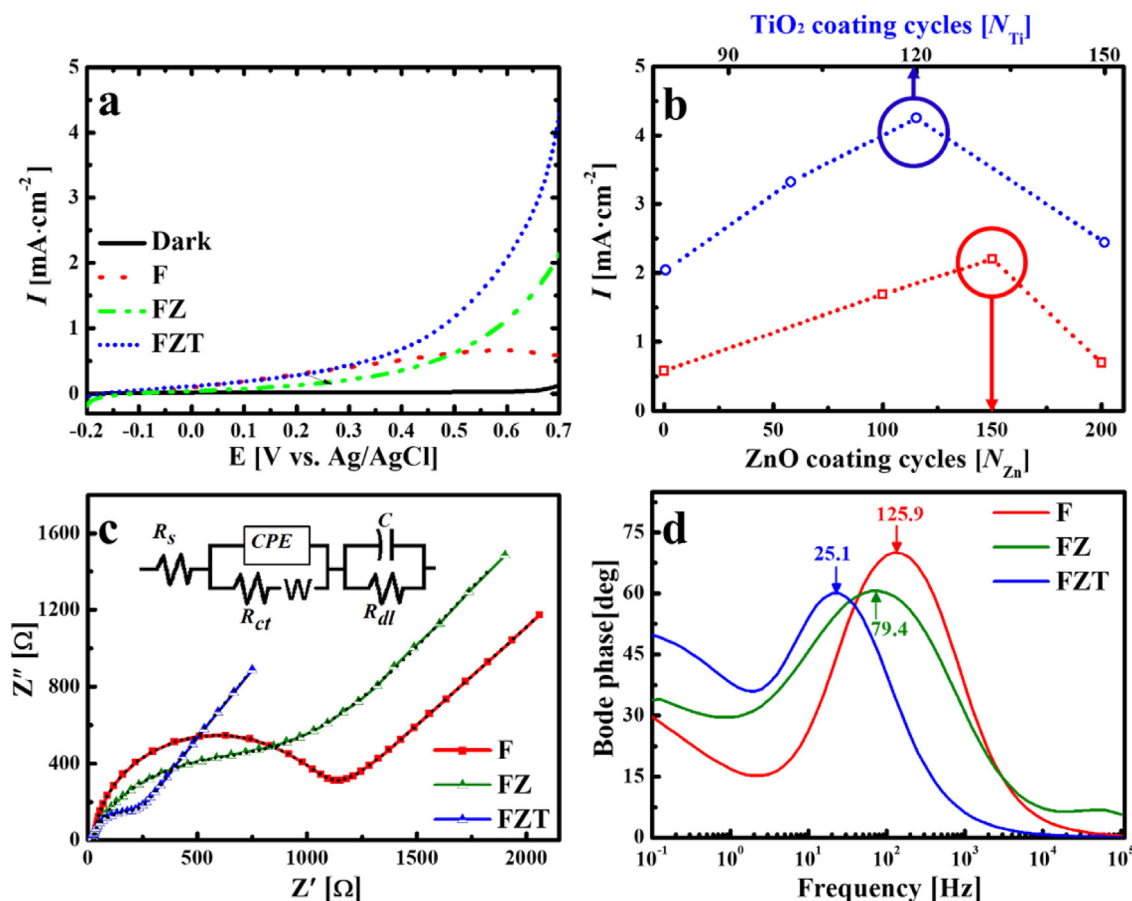


Fig. 6. (a) Current density vs. voltage curves of Fe_2O_3 (F), $\text{Fe}_2\text{O}_3/\text{ZnO}$ (FZ), and $\text{Fe}_2\text{O}_3/\text{ZnO}/\text{TiO}_2$ (FZT). (b) Changes in photocurrent with variations in thicknesses of ZnO layer formed over F and TiO_2 layer formed over FZ ($N_{\text{Zn}} = 150$) at 0.7 V. Electrochemical impedance spectra of samples F, FZ, and FZT: (c) Nyquist plot with equivalent circuit used for fitting (inset) and (d) Bode phase plots.

Table 1

PEC performances of previously reported passivated/overlayer Fe_2O_3 films as compared with fabricated FZT films in this study.

Materials	Reaction solution	PCD [mA/cm^2]	References
Fe_2O_3	1.0 M KOH	1.3 ^a	[2]
$\text{Fe}_2\text{O}_3/\text{TiO}_2$	1.0 M NaOH	1.2 ^b	[8]
$\text{Fe}_2\text{O}_3/\text{TiO}_2$	1.0 M KOH	2.0 ^b	[11]
$\text{Fe}_2\text{O}_3/\text{TiO}_2$	1.0 M NaOH	2.0 ^b	[13]
$\text{Fe}_2\text{O}_3/\text{TiO}_2$	1.0 M NaOH	0.6 ^b	[14]
$\text{TiO}_2/\text{Fe}_2\text{O}_3$	1.0 M NaOH	0.4 ^b	[16]
$\text{Fe}_2\text{O}_3/\text{ZnO}/\text{TiO}_2$	1.0 M NaOH	4.25^c	Present

PCD value at: 0.6 V vs Ag/AgCl^a, 1.23 V vs RHE^b, 0.7 V vs Ag/AgCl^c.

than was observed in other studies.

EIS analysis was performed to characterize the resistances between the electrode and electrolyte during the electrochemical process without having to destroy the samples. The obtained Nyquist data for samples F, FZ, and FZT are shown in Fig. 6c. Further, the acquired impedance data for these samples were fit to an equivalent circuit model (see inset of Fig. 6c); the various components of the circuit are listed in Table 2. The resistance associated with the system, as indicated in the equivalent circuit, are the solution resistance (R_s), charge-transfer resistance (R_{ct}), and electrical double layer resistance (R_{dl}). The electrical double layer at the electrode/electrolyte interface has a determining effect on the oxide–electrolyte interactions and hence the PEC performance. The lower charge-transfer resistance of the heterostructure results in

Table 2

Various components of Randles equivalent circuits for Fe_2O_3 , $\text{Fe}_2\text{O}_3/\text{ZnO}$, and $\text{Fe}_2\text{O}_3/\text{ZnO}/\text{TiO}_2$ films under dark and light conditions.

Components	F	FZ	FZT
Nyquist plot fitting data			
R_s (Ω)	32.3	16.8	18.4
R_{sc} (Ω)	1.8	146.3	19.4
R_{ct} (Ω)	983.9	539.4	178.2
C_{sc} (F)	6.9×10^{-6}	3.1×10^{-5}	1.3×10^{-4}
CPE ($S-s^n$)	6.96×10^{-5}	3.1×10^{-4}	6.0×10^{-4}
W ($S-s^{0.5}$)	7.7×10^{-4}	9.8×10^{-6}	7.5×10^{-4}
Bode phase data			
Frequency (Hz)	126	79	25
Photoelectron lifetime (ms)	1.3	2.0	6.3

faster ionic transfer, thus enhancing the PEC performance of the photoanode. The double-layer capacitance (C_{dl}) at the electrolyte/electrode interface, the Warburg diffusion impedance (W), and the constant phase element (CPE) were as shown in the equivalent circuit inset in Fig. 6c. The heterostructured film exhibited lower R_s and R_{ct} values compared to those of the pristine Fe_2O_3 sample.

The Bode phase plot shows peaks related to charge transfer at the photoanode–electrolyte interface. The characteristic oscillation frequency (f_c) at which the phase angle is a maximum is inversely proportional to the electron lifetime (τ_e) under illumination, as indicated by the expression $\tau_e = 1/(2\pi f_c)$. The Bode plots for samples F, FZ, and FZT are given in Fig. 6d, which shows the variations in the characteristic frequency at the peak phase values.

Sample F shows the lowest photoelectron lifetime (1.3 ms), with those of FZ and FZT being 2.0 and 6.2 ms, respectively. The longer photoelectron lifetime in FZT can be attributed to carrier confinement at the $\text{Fe}_2\text{O}_3/\text{ZnO}$ interface because of the ultrathin ZnO layer sandwiched between the Fe_2O_3 and TiO_2 layers [32,33]. In addition, Fe_2O_3 has intermediate defects, at which the electron–hole pairs can recombine rapidly [16]. Thus, the presence of the ZnO/TiO_2 films on the Fe_2O_3 layer induces fast charge transfer and enhanced electron–hole separation and increases the recombination lifetime.

The PEC performance of the Fe_2O_3 film coated with the ZnO/TiO_2 layers (FZT) using ALD was tested under chronoamperometric conditions. We observed that the PCD decreased very marginally over 1000 s at 0.5 V (vs. Ag/AgCl), as shown in Fig. 7a. The generation of a stable photocurrent during water oxidation can be attributed to the TiO_2 coating. The ON and OFF durations were kept at 50 s for each cycle. The rapid increase in the current density as soon as the light was incident on the sample and the sharp fall in the current to $-0.05 \text{ mA}/\text{cm}^2$ confirmed that the sample exhibited fast charge-transfer characteristics and excellent photoactivity. Furthermore, the fact that the peak PCD value remained unchanged for 1000 s indicated that the TiO_2 layer successfully prevented photocorrosion of the underlying photocatalytic materials (Fe_2O_3 and ZnO). However, the on-off data for the pure Fe_2O_3 case indicates some degradation in PCD at later times, as shown in Fig. 7a. In addition, the absolute value of PCD for the pure Fe_2O_3 is also lower, as compared to the passivated films. Thus, it is confirmed that TiO_2 passivation enhances both photocurrent density and stability of the films.

The stabilities of samples F (Fe_2O_3) and FZT ($\text{Fe}_2\text{O}_3/\text{ZnO}/\text{TiO}_2$) were measured at a constant applied potential of 0.6 V. Sample FZT was tested for long-term stability and exhibited stable performance

for 20000 s (see Fig. 7b). In contrast, the Fe_2O_3 sample, which did not have any passivation layer (i.e., sample F), showed a lower current response, which gradually decreased over the first 50 s and then plateaued, as shown in Fig. S3. Moreover, this sample remained stable only for 1140 s, after which it underwent significant oxidation, exhibiting large fluctuations in its photocurrent. The inset of Fig. 7b shows the amount of O_2 evolved as measured using a simple lab-built system along with a photograph of the generated O_2 bubbles (see Movie S1) as evidence of O_2 evolution.

Supplementary video related to this article can be found at <https://doi.org/10.1016/j.jallcom.2019.05.255>.

That H_2 and O_2 were generated was confirmed by identifying the gases after isolating them and measuring their volumes (volume of H_2 was 5.1 mL and that of O_2 was 2.4 mL; see Movie S1). Faradaic efficiency was obtained from the static test, detection, and quantification of the product (here O_2). Faradaic efficiency is defined as the ratio of total charge transferred that produces O_2 evolution to the total charge consumed during the static photoelectrochemical measurements. The Faradaic efficiency for O_2 evolution under light-driven water splitting was determined using Eq. (1) and was found to be approximately 98% [34].

$$\eta_F = \frac{V_{\text{actual}}}{V_{\text{theo}}} = \frac{V_{\text{actual}}}{(N_O \cdot Q \cdot V_m) / (N \cdot F)} \quad (1)$$

where V_{actual} is the volume of O_2 collected during the experiment (see movie S1) while V_{theo} is the theoretical volume of O_2 evolved based upon the measured photocurrent. N_O is the number of moles of oxygen per mole of H_2O (for O, $N_O = 1$), and Q is the total charge as determined by integrating the current over time. Finally, V_m , N , and F are the molar volume of an ideal gas (22.4 L/mol at 293 K and

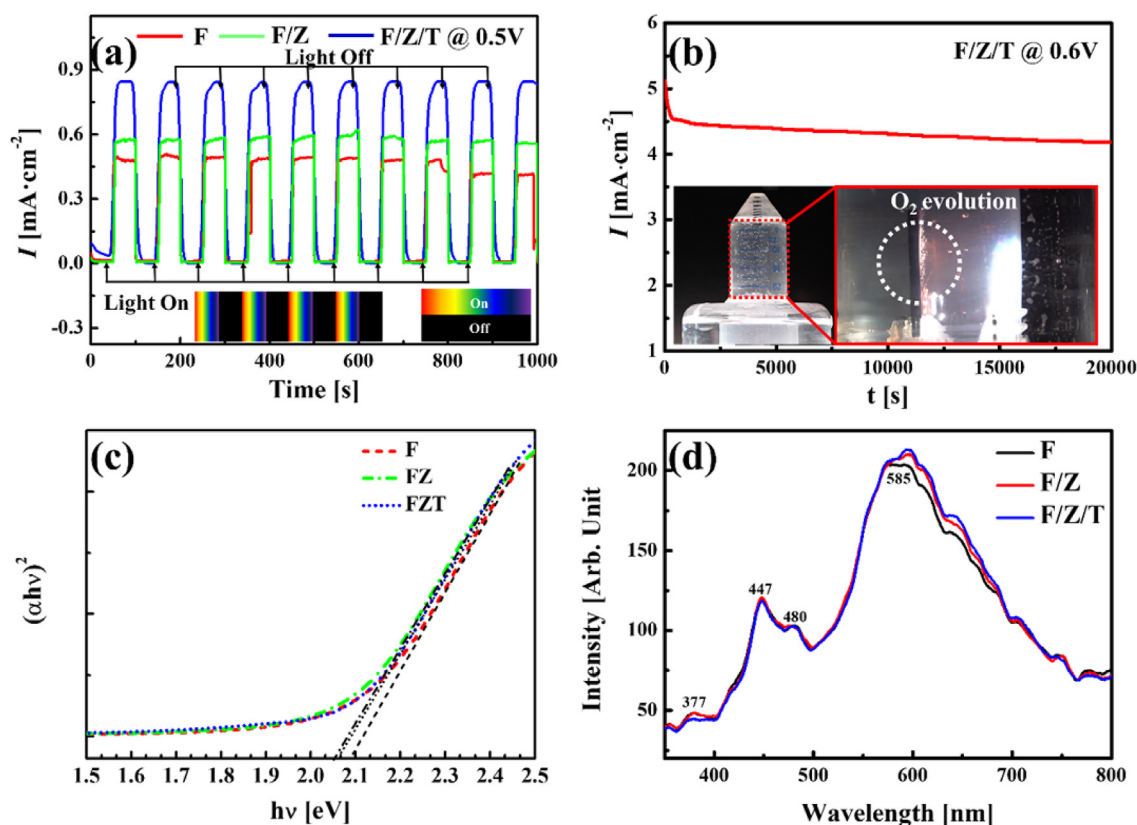


Fig. 7. (a) Transient photocurrent responses of F, FZ and FZT photoanode to ON-OFF illumination, (b) long-term PEC performance of FZT photoelectrode at 0.6 V (inset image shows O_2 evolution), (c) Tauc plot of $(\alpha h\nu)^2$ vs. $h\nu$, and (d) photoluminescence spectra of samples F, FZ, and FZT.

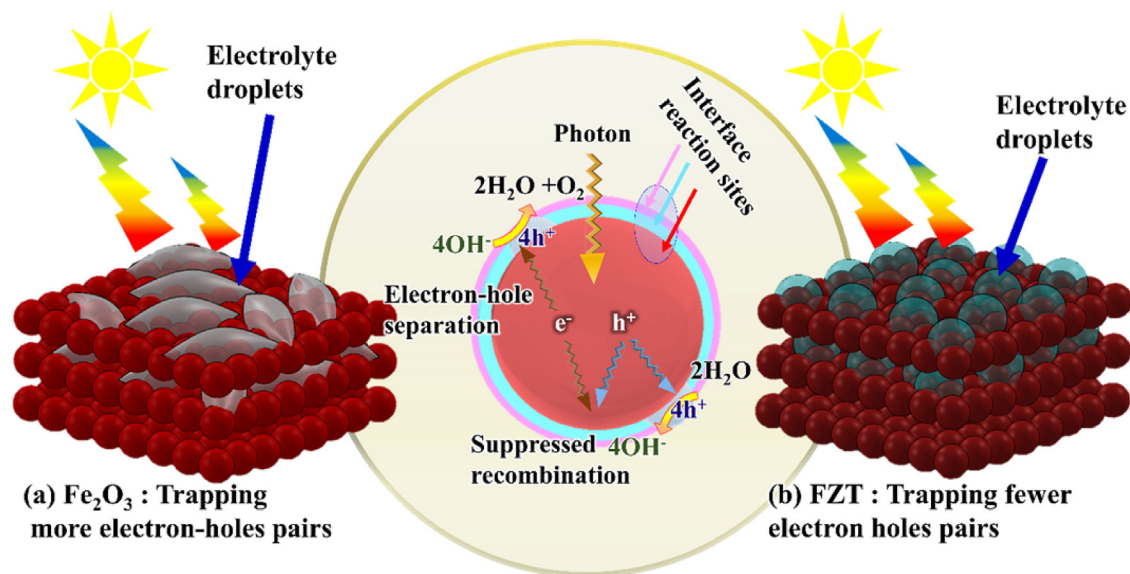


Fig. 8. Photoelectrochemical water splitting mechanism schematic: (a) Fe_2O_3 surface with elliptical electrolyte droplets and (b) FZT surface with spherical shaped electrolyte droplets. The central drawing indicates the O_2 evolution process under illuminated condition over the FZT surface.

1 atm), number of electrons per mole of H_2O ($N=4$), and the Faraday constant ($F=96485\text{ C mol}^{-1}$), respectively. In order to elucidate the reason for the superior performance of FZT, a Tauc plot was prepared (see Fig. 7c) from the absorbance spectra shown in Fig. S4. The bandgap value as determined from the Tauc plot was 2.1 eV for the Fe_2O_3 sample and ~ 2.06 eV for the $\text{Fe}_2\text{O}_3/\text{ZnO}$ and $\text{Fe}_2\text{O}_3/\text{ZnO}/\text{TiO}_2$ samples [35]. The optical bandgap (E_g) value was determined by extrapolating the absorption edge, as given by Eq. (2):

$$\alpha = \frac{2.303A}{d} \quad (2)$$

where α is the absorption coefficient, A is the absorbance, and d is the sample thickness.

Further, Fig. 7d shows the photoluminescence (PL) spectra of samples F, FZ, and FZT under 325 nm illumination. The spectra exhibit peaks at 377, 447, 480, 585, and 855 nm [36]. Fluorescence occurs near the UV (377 nm) and blue violet (400–485 nm) regions. The emission peaks at 447 and 480 nm can be attributed to the radiative recombination of excitons [37]. The photoemission peak at approximately 585 nm matches the bandgap of Fe_2O_3 (2.14 eV). Moreover, the intensity of the peak at 377 nm was higher in the cases of FZ and FZT, reflecting the presence of the materials with UV bandgap energies (ZnO/TiO_2) in these samples. Finally, the increase in the intensity of the peak at 585 nm in the cases of FZ and FZT as well as the broadening of this peak was related to the surface passivation of Fe_2O_3 by the ZnO/TiO_2 layers [38,39].

A schematic of the mechanism responsible for the photochemical properties of Fe_2O_3 and $\text{Fe}_2\text{O}_3/\text{ZnO}/\text{TiO}_2$ is shown in Fig. 8, illustrating the PEC phenomenon that occurs at the semiconductor/electrolyte interface. As can be seen in Fig. 3b, the contact angle of the Fe_2O_3 film is relatively small, and the film has a lower surface roughness (see Fig. 3e), owing to which the degree of adsorbed species coverage of the film surface is greater. This causes a greater number of holes to be trapped; these holes then readily recombine with the free electrons generated under illumination. After long-term cycling, the wettability of both the Fe_2O_3 and $\text{Fe}_2\text{O}_3/\text{ZnO}/\text{TiO}_2$ films is enhanced, as can be seen from Fig. S5. This increased

wettability has an adverse effect on the PEC performance because it promotes rapid charge transfer and oxidation. Sample FZT was protected by the TiO_2 passivation layer and was able to produce stable performance with one-way hole transfer reaction at the electrode-electrolyte interface. In addition, the degree of hole trapping is relatively lower when the electrolyte contact area is small (Fig. 8, see schematic of FZT on right). Thus, the holes available at the surface participate in water oxidation, ultimately suppressing electron-hole recombination. These phenomena are responsible for the PCD value of FZT being higher (see Fig. 6b).

4. Conclusions

In this study, we observed that the photocurrent of Fe_2O_3 films (0.5 mA cm^{-2}) improves significantly, to 4.25 mA cm^{-2} , after their surface modification with an ultrathin ALD-based ZnO/TiO_2 coating. The passivation process reduces the number of surface defects, limiting the trapping of holes. The passivation layers exhibited stable performance with one-way hole transfer reaction at the electrode-electrolyte interface. As a result, water oxidation was promoted. The availability of holes at the surface and their rapid participation in water splitting suppresses electron-hole recombination. The ~ 4.8 -fold increase in the lifetime of photo-generated charge carriers relative to that in the pristine Fe_2O_3 sample further demonstrated the effect of the surface passivation of Fe_2O_3 . In the future, we aim to realize an anodic shift in the onset potential. The results of this study suggest that cold-spray-coated Fe_2O_3 photoanodes passivated with ZnO/TiO_2 show significantly reduced surface recombination rates and substantially enhanced PEC performances.

Acknowledgement

This research was supported by the Technology Development Program to Solve Climate Changes of the National Research Foundation (NRF) funded by the Ministry of Science, ICT & Future Planning (NRF-2016M1A2A2936760) and NRF-2017R1A2B4005639, NRF-2013R1A5A1073861.

Appendix A. Supplementary data

Supplementary data to this article can be found online at <https://doi.org/10.1016/j.jallcom.2019.05.255>.

References

- [1] S. Selvaraj, H. Moon, D.-H. Kim, Synthesis and photo-electrochemical properties of spinel-ferrite-coated hematite for solar water splitting, *Appl. Surf. Sci.* 429 (2018) 42–47.
- [2] N.T. Hahn, H. Ye, D.W. Flaherty, A.J. Bard, C.B. Mullins, Reactive ballistic deposition of α -Fe₂O₃ thin films for photoelectrochemical water oxidation, *ACS Nano* 4 (2010) 1977–1986.
- [3] H. Yoon, M.G. Mali, J.Y. Choi, M.-w. Kim, S.K. Choi, H. Park, S.S. Al-Deyab, M.T. Swihart, A.L. Yarin, S.S. Yoon, Nanotextured pillars of electrosprayed bismuth vanadate for efficient photoelectrochemical water splitting, *Langmuir* 31 (2015) 3727–3737.
- [4] Z.-F. Huang, L. Pan, J.-J. Zou, X. Zhang, L. Wang, Nanostructured bismuth vanadate-based materials for solar-energy-driven water oxidation: a review on recent progress, *Nanoscale* 6 (2014) 14044–14063.
- [5] K.L. Hardee, A.J. Bard, Semiconductor electrodes: V. The application of chemically vapor deposited iron oxide films to photosensitized electrolysis, *J. Electrochem. Soc.* 123 (1976) 1024–1026.
- [6] K. Zhang, T. Dong, G. Xie, L. Guan, B. Guo, Q. Xiang, Y. Dai, L. Tian, A. Batool, S.U. Jan, R. Boddula, A.A. Thebo, J.R. Gong, Sacrificial interlayer for promoting charge transport in hematite photoanode, *ACS Appl. Mater. Interfaces* 9 (2017) 42723–42733.
- [7] Gurudayal, P.S. Bassi, T. Sriharan, L.H. Wong, Recent progress in iron oxide based photoanodes for solar water splitting, *J. Phys. D Appl. Phys.* 51 (2018) 473002.
- [8] M.G. Ahmed, I.E. Kretschmer, T.A. Kandel, A.Y. Ahmed, F.A. Rashwan, D.W. Bahnemann, A facile surface passivation of hematite photoanodes with TiO₂ overlayers for efficient solar water splitting, *ACS Appl. Mater. Interfaces* 7 (2015) 24053–24062.
- [9] T.S. David, C. Maurin, S. Kevin, G. Michael, Light-induced water splitting with hematite: improved nanostructure and iridium oxide catalysis, *Angew. Chem.* 122 (2010) 6549–6552.
- [10] T. Hisatomi, F. Le Formal, M. Cornuz, J. Brillet, N. Tétreault, K. Sivula, M. Grätzel, Cathodic shift in onset potential of solar oxygen evolution on hematite by 13-group oxide overlayers, *Energy Environ. Sci.* 4 (2011) 2512–2515.
- [11] T.H. Jeon, G.-h. Moon, H. Park, W. Choi, Ultra-efficient and durable photoelectrochemical water oxidation using elaborately designed hematite nanorod arrays, *Nano Energy* 39 (2017) 211–218.
- [12] K.M.H. Young, T.W. Hamann, Enhanced photocatalytic water oxidation efficiency with Ni(OH)₂ catalysts deposited on α -Fe₂O₃ via ALD, *Chem. Commun. (Camb)* 50 (2014) 8727–8730.
- [13] B. Davide, C. Giorgio, G. Alberto, M. Chiara, Michael EA. Warwick, K. Kimmo, S. Cinzia, T. Stuart, G. Yakup, R. Tero-Petri, B. Laura, B. Elza, V.T. Gustaaf, L. Helge, M. Sanjay, Fe₂O₃-TiO₂ nano-heterostructure photoanodes for highly efficient solar water oxidation, *Adv. Mater. Interfaces* 2 (2015) 1500313.
- [14] X. Yang, R. Liu, C. Du, P. Dai, Z. Zheng, D. Wang, Improving hematite-based photoelectrochemical water splitting with ultrathin TiO₂ by atomic layer deposition, *ACS Appl. Mater. Interfaces* 6 (2014) 12005–12011.
- [15] M. Liu, C.-Y. Nam, C.T. Black, J. Kamcev, L. Zhang, Enhancing water splitting activity and chemical stability of zinc oxide nanowire photoanodes with ultrathin titania shells, *J. Phys. Chem. C* 117 (2013) 13396–13402.
- [16] C. Zhang, Q. Wu, X. Ke, J. Wang, X. Jin, S. Xue, Ultrathin hematite films deposited layer-by-layer on a TiO₂ underlayer for efficient water splitting under visible light, *Int. J. Hydrogen Energy* 39 (2014) 14604–14612.
- [17] S. Ludmilla, H.C. Isaac, G. Sixto, F.S. Francisco, B. Juan, T.S. David, G. Michael, Understanding the role of underlayers and overlayers in thin film hematite photoanodes, *Adv. Funct. Mater.* 24 (2014) 7681–7688.
- [18] J.-G. Lee, D.-Y. Kim, B. Kang, D. Kim, H.-e. Song, J. Kim, W. Jung, D. Lee, S.S. Al-Deyab, S.C. James, S.S. Yoon, Nickel-copper hybrid electrodes self-adhered onto a silicon wafer by supersonic cold-spray, *Acta Mater.* 93 (2015) 156–163.
- [19] D. Wang, Y. Chen, Y. Zhang, X. Zhang, N. Suzuki, C. Terashima, Boosting photoelectrochemical performance of hematite photoanode with TiO₂ underlayer by extremely rapid high temperature annealing, *Appl. Surf. Sci.* 422 (2017) 913–920.
- [20] J. Yuan, X. Zhang, C. Chen, Y. Hao, R. Agrawal, C. Wang, W. Li, H. Yu, Y. Yu, X. Zhu, Facile fabrication of three-dimensional porous ZnO thin films on Ni foams for lithium ion battery anodes, *Mater. Lett.* 190 (2017) 37–39.
- [21] A.M. Jubb, H.C. Allen, Vibrational spectroscopic characterization of hematite, maghemite, and magnetite thin films produced by vapor deposition, *ACS Appl. Mater. Interfaces* 2 (2010) 2804–2812.
- [22] B.M. Klahr, A.B.F. Martinson, T.W. Hamann, Photoelectrochemical investigation of ultrathin film iron oxide solar cells prepared by atomic layer deposition, *Langmuir* 27 (2010) 461–468.
- [23] C. Yilmaz, U. Unal, Morphology and crystal structure control of α -Fe₂O₃ films by hydrothermal-electrochemical deposition in the presence of Ce³⁺ and/or acetate, F⁻ ions, *RSC Adv.* 6 (2016) 8517–8527.
- [24] P.M. Kulal, D.P. Dubal, C.D. Lokhande, V.J. Fulari, Chemical synthesis of Fe₂O₃ thin films for supercapacitor application, *J. Alloys Compd.* 509 (2011) 2567–2571.
- [25] Y. Li, X. Wei, B. Zhu, H. Wang, Y. Tang, T.C. Sum, X. Chen, Hierarchically branched Fe₂O₃@TiO₂ nanorod arrays for photoelectrochemical water splitting: facile synthesis and enhanced photoelectrochemical performance, *Nanoscale* 8 (2016) 11284–11290.
- [26] B. Bharti, S. Kumar, H.-N. Lee, R. Kumar, Formation of oxygen vacancies and Ti³⁺ state in TiO₂ thin film and enhanced optical properties by air plasma treatment, *Sci. Rep.* 6 (2016) 32355.
- [27] J.-G. Lee, B.N. Joshi, J.-H. Lee, T.-G. Kim, D.-Y. Kim, S.S. Al-Deyab, I.W. Seong, M.T. Swihart, W.Y. Yoon, S.S. Yoon, Stable high-capacity lithium ion battery anodes produced by supersonic spray deposition of hematite nanoparticles and self-healing reduced graphene oxide, *Electrochim. Acta* 228 (2017) 604–610.
- [28] H.J. Cui, J.K. Cai, H. Zhao, B. Yuan, C. Ai, M.L. Fu, One step solvothermal synthesis of functional hybrid gamma-Fe₂O₃/carbon hollow spheres with superior capacities for heavy metal removal, *J. Colloid Interface Sci.* 425 (2014) 131–135.
- [29] B. Joshi, E. Samuel, M.-W. Kim, S. Park, M.T. Swihart, W.Y. Yoon, S.S. Yoon, Atomic-layer-deposited TiO₂-SnZnO/carbon nanofiber composite as a highly stable, flexible and freestanding anode material for lithium-ion batteries, *Chem. Eng. J.* 338 (2018) 72–81.
- [30] R. Rajendran, Z. Yaakob, M.A. Mat Teridi, M.S. Abd Rahaman, K. Sopian, Preparation of nanostructured p-NiO/n-Fe₂O₃ heterojunction and study of their enhanced photoelectrochemical water splitting performance, *Mater. Lett.* 133 (2014) 123–126.
- [31] M.-W. Kim, K. Kim, T.Y. Ohm, H. Yoon, B. Joshi, E. Samuel, M.T. Swihart, S.K. Choi, H. Park, S.S. Yoon, Electrosprayed BiVO₄ nanopillars coated with atomic-layer-deposited ZnO/TiO₂ as highly efficient photoanodes for solar water splitting, *Chem. Eng. J.* 333 (2018) 721–729.
- [32] A. Seza, F. Soleimani, N. Naseri, M. Soltaninejad, S.M. Montazeri, S.K. Sadrnezhad, M.R. Mohammadi, H.A. Moghadam, M. Forouzandeh, M.H. Amin, Novel microwave-assisted synthesis of porous g-C₃N₄/SnO₂ nanocomposite for solar water-splitting, *Appl. Surf. Sci.* 440 (2018) 153–161.
- [33] Y. Zhang, F. Liu, End to end assembly of CaO and ZnO nanosheets to propeller-shaped architectures by orientation attachment approaches, *J. Cryst. Growth* 420 (2015) 94–100.
- [34] H.-S. Jo, M.-W. Kim, B. Joshi, E. Samuel, H. Yoon, M.T. Swihart, S.S. Yoon, Ni-core CuO-shell fibers produced by electrospinning and electroplating as efficient photocathode materials for solar water splitting, *Nanoscale* 10 (2018) 9720–9728.
- [35] H. Feng, Y. Wang, C. Wang, F. Diao, W. Zhu, P. Mu, L. Yuan, G. Zhou, F. Rosei, Defect-induced enhanced photocatalytic activities of reduced α -Fe₂O₃ nanoblades, *Nanotechnology* 27 (2016) 295703.
- [36] P. Shikha, B.S. Randhawa, T.S. Kang, Greener synthetic route for superparamagnetic and luminescent α -Fe₂O₃ nanoparticles in binary mixtures of ionic liquid and ethylene glycol, *RSC Adv.* 5 (2015) 51158–51168.
- [37] R. Fu, W. Wang, R. Han, K. Chen, Preparation and characterization of γ -Fe₂O₃/ZnO composite particles, *Mater. Lett.* 62 (2008) 4066–4068.
- [38] Q. Wu, G. Wu, L. Wang, W. Hu, H. Wu, Facile synthesis and optical properties of Prussian Blue microcubes and hollow Fe₂O₃ microboxes, *Mater. Sci. Semicond. Process.* 30 (2015) 476–481.
- [39] S. Chakrabarti, D. Ganguli, S. Chaudhuri, Optical properties of γ -Fe₂O₃ nanoparticles dispersed on sol-gel silica spheres, *Phys. E Low-dimens. Syst. Nanostruct.* 24 (2004) 333–342.